Observation of correlations in tunneling of surface-state electrons

S. Yücel, L. Menna, and E. Y. Andrei
Department of Physics and Astronomy, Rutgers University, Piscataway, New Jersey 08855
(Received 29 June 1992; revised manuscript received 23 March 1992)

We measured the escape rates of surface-state electrons from an electron layer confined at the liquid-helium–vacuum interface in the temperature range of 30–450 mK, for densities $(0.02–2.2)\times10^8$ cm^{-2}. We compared the measured escape rates with calculated tunneling rates in a model where the interactions between the escaping electron and the other electrons are described by an effective single-particle potential. Below 200 mK the escape rates were temperature independent. The single-particle rates were enhanced exponentially as the density was increased up to a critical density n_c. In this regime the calculated and measured rates were in good agreement. At n_c we observe a one order of magnitude steep rise and the time development of density becomes extremely nonlinear. We show that this nonlinearity can be explained by the electron impact excitation of helium atoms on the walls of the cell. As the barrier is raised so that the escape rates decrease below 5.0×10^{-4} sec^{-1}, a new mechanism seems to dominate the escape and the rates become very weakly density and external field dependent. Thermally activated escape was observed above 250 mK and the activation energies were in good agreement with the calculated values.

I. INTRODUCTION

Tunneling of a particle whose motion under the barrier is modified by the interactions with other systems has received an increasing amount of attention over the past decade. Its importance in the operation of tunneling electron microscopes,[1] Josephson junctions,[2] tunneling devices,[3] as well as in the physics of correlated electron systems on dielectric surfaces[4–7] and in heterostructures[8] renders this problem of broad practical interest. Although theoretical work concerning the dynamical aspects of tunneling is quite abundant,[9] detailed experimental studies on well-characterized systems remain very few.

Recently we reported the observation of tunneling out of a layer of electrons bound to a liquid-helium surface.[4] This system is ideally suited for studying the dynamical aspects of tunneling due to its exceptional experimental flexibility. Some of its unique features are a well-defined and tunable potential barrier, interactions which can be dialed in gradually, and an observable single electron tunneling limit. In this paper we give a detailed account of these experiments and present additional data.

The paper is organized as follows. In Sec. II we discuss the current issues associated with tunneling in the presence of interactions. In Sec. III we describe the system of surface-state electrons (SSE), the experimental cell, the detection methods, and procedures for analyzing the data. In Sec. IV we present our results and discuss the density, temperature, and external electric-field dependence of the escape rates.

II. TUNNELING AND CORRELATIONS

Correlations play an important role in the physics of electron layers and are responsible for many interesting phenomena such as the fractional quantum Hall effect and the Wigner crystallization. The phase of the system is determined by the interplay between three energies:[10] the correlation energy $V_c=e^2/\sqrt{\pi n}$, the thermal energy kT, and the Fermi energy $E_F=\hbar^2\pi n/m$, where n, m, and e are the two-dimensional (2D) electronic density, mass, and charge, respectively. In the presence of a magnetic field, the magnetic energy $\hbar\omega_c$ plays a role in determining the various magnetic phases, where ω_c is the cyclotron frequency. In this paper we consider only the classical regime $E_F \ll kT$, whose phase boundary is determined by the classical ordering parameter $\Gamma=V_c/kT$. When the Coulomb correlation energy is much smaller than the thermal energy, $\Gamma \ll 1$, the system is in an uncorrelated gas phase. As Γ increases correlations become more important and at $\Gamma^C=127\pm3$ the electrons solidify into a Wigner crystal.[11] In the quantal regime $E_F \geq kT$, the thermodynamics of the system is determined by the quantal ordering parameter $r_s=V_c/E_F \propto n^{-1/2}$. Monte Carlo calculations[12] predict the melting of the quantum Wigner crystal at $r_s^Q=37$.

Correlations also affect the motion perpendicular to the surface: evaporation and tunneling.[4–7,13,14] With surface-state electrons these effects can be studied over a wide temperature and density range covering the classical solid and liquid phases as well as the boundary between them. Iye *et al.*[13] used a simple model to account for the correlations in their measured thermally activated rates. According to this model, which we will refer to as the correlation hole model (CHM), each electron excludes all neighboring electrons from a disk of radius r_0 (correlation hole) whose size is obtained from the relation $g(r_0)=0.5$, where $g(r)$ is the pair-correlation function.[15] The resulting effective potential is that arising from a continuous charge sheet pierced by a hole whose radius r_0 shrinks as the electron moves out of the surface and closes at a distance r_0 above the plane. More recently

Goodkind *et al.*[7] measured escape rates and the thermal activation energies in the density range $n=(3\times10^7)-(5\times10^8)$ cm^{-2} and also found that the CHM accounts well for the thermally activated processes. Below 0.5 K, their escape rates became temperature independent and therefore were attributed to tunneling out of the ground state.[7] But these temperature-independent rates were up to 50 orders of magnitude larger than calculated tunneling rates in the CHM.[5] This enormous discrepancy raised questions about the applicability of a single-particle approach to the decay of this many-body system. Correlations were treated in a more rigorous way by Vil'k and Monarkha,[16] who used a harmonic lattice approximation (HLA) to determine the potential energy of an electron above a triangular electron lattice. For the temperature and density regime explored by most experiments, there is good agreement between the potential of the CHM and that obtained in the HLA. In this paper we compare our results to the CHM only because of its simple analytical form.

At sufficiently high densities, however, the escape from the surface can no longer be viewed as a single-particle problem, and a theory of tunneling of two-dimensional electrons should take into account the many-body effects as well as the interactions with the thermal baths and external fields. Such a general theory does not yet exist and therefore approximate methods are needed. A simple approach is to assume that one electron at a time tunnels and the correlation effects can be incorporated into a static effective potential as was done in the CHM. This approximation is expected to break down when the characteristic time scale of tunneling is longer than the response time of the two-dimensional electrons because the hole left by the tunneling electron in the charge sheet may close during the escape and modify the barrier significantly.

The possibility of observing the dynamical response of the barrier focused attention on the question of how long it takes for an electron to tunnel. The tunneling time of both quasibound and scattering electrons was studied extensively over the past decade. Although some consensus as to its definition has arisen, there still exist competing points of view regarding its interpretation.[9] A tunneling time for a bound electron in the context of ionization in intense laser fields was introduced by Keldysh.[17] Recently Yücel and Andrei[18,19] studied the ionization of SSE in time-dependent fields and showed that the tunneling time of SSE is the same as the Keldysh time and its inverse is the real positive expectation value of an operator. The surface-state electrons are well suited for studying these questions since both the tunneling time and the response time of the electrons can be varied independently over wide overlapping ranges. In other electronic systems the tunneling time is usually much shorter than the response time of the many-body system. In heterostructures, for example, the tunneling time is typically 1 ps or less,[8] while in atomic systems and tunneling electron microscopes[20] it is $10^{-14}-10^{-15}$ s as compared to 10–100 ps in SSE.

III. EXPERIMENT

A. Surface-state electrons

An electron above liquid helium is attracted to the surface by the Coulomb potential of its image charge but is prevented from entering the liquid by a 1-eV barrier.[21] If this barrier is made infinitely high the surface-state electron may be thought of as a one-dimensional hydrogen atom with a scaled nuclear charge $Q=[(\epsilon-1)/4(\epsilon+1)]e$, where $\epsilon=1.0572$ is the dielectric constant of the liquid helium. The electronic energy for motion perpendicular to the helium surface is quantized in a Rydberg series[21,22] with a ground-state energy of $E_B=7.6$ K. Its wave function in the ground state describes an electron free to move in a plane parallel to the liquid-helium surface at a distance of 114 Å above it. The superfluid helium substrate is inert and appears completely smooth at these temperatures since the root-mean-square fluctuation amplitude of the surface, ~1 Å, is much less than the distance between the electron and the helium surface. The electronic motion within the 2D layer is affected only by the interaction with capillary waves (ripplons) and with helium atoms in the vapor. At temperatures $T<0.7$ K, where the helium vapor pressure is negligible, electron-ripplon interactions are the main scattering mechanism. These interactions are sufficiently weak so as not to change the electronic mass for small pressing

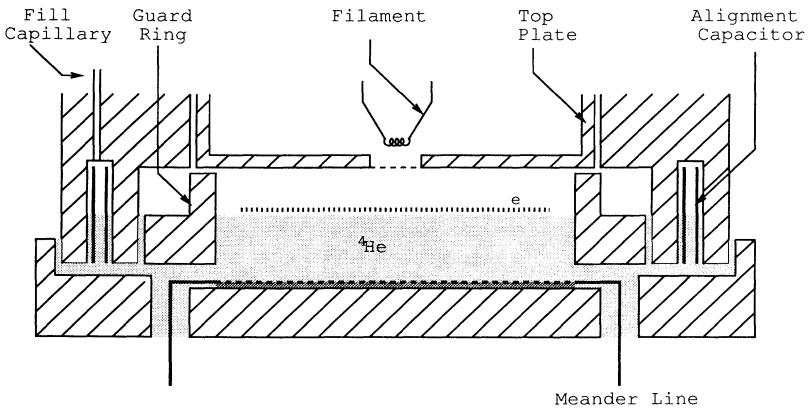

FIG. 1. The schematics of the cell. The drawings are not to scale and some details were omitted for clarity.

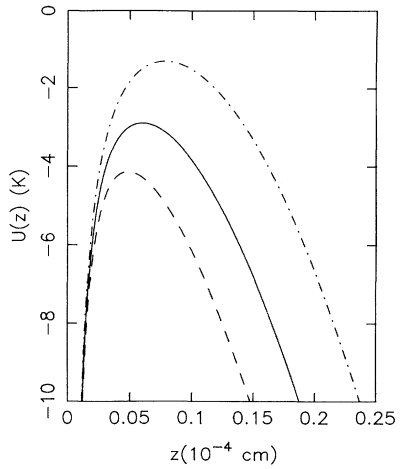

FIG. 2. The barrier seen by electron tunneling out of a layer of density $n=10^8$ cm^{-2} for several values of the applied voltage: solid line, $V_t=0.0$ V; dashed line, $V_t=+5.0$ V; dot-dashed line, $V_t=-5.0$ V. The correlation hole potential (12) is used to determine the barrier.

fields.[23] Their effect is described in terms of a mobility which is exceptionally high, $\mu\sim10^7$ cm^2/V s, reflecting the fact that the electronic motion within the layer is essentially free.

In a typical experiment the surface-state electrons (SSE) are pressed toward the helium surface by an external field created between two metal plates which are parallel to the electron layer that is placed between them (Fig. 1). For distances large compared to the interelectronic spacing a, the electric field above the electron sheet has three components: the repulsive field arising from the uniform charge sheet $\mathcal{E}_c=-2\pi ne$, the external pressing field $\mathcal{E}_p=-V_t/(d/\epsilon+h)$, and the attractive field of the positive image charges of the electrons on the metal plates $\mathcal{E}_i=(d-\epsilon h/\epsilon h+d)\mathcal{E}_c$. Here the helium level d is measured from the bottom plate and V_t is the voltage difference between the top and bottom plates which are separated by a distance $D=h+d$ (Fig. 1). Thus, at large distances $z\gg1/\sqrt{\pi n}$ the potential energy of an electron is

$$\lim_{z\to\infty} U(z)=-\frac{Qe}{z}+e(\mathcal{E}_p+\mathcal{E}_c+\mathcal{E}_i)z\ , \tag{1}$$

where the first term arises from the interaction between the helium substrate and the electron and z is the distance to the electron layer. At low temperatures, when $\mathcal{E}_p$ is reduced so that the total field $(\mathcal{E}_p+\mathcal{E}_c+\mathcal{E}_i)<0$, the electrons are confined by a finite potential barrier through which they can escape by tunneling. The size of the barrier can thus be tuned with the applied voltage V_t, as illustrated in Fig. 2. At higher temperatures, thermally activated processes will also contribute to the escape.

B. The cell

The experimental cell consists of a guard ring of radius $R=9.0$ mm placed between two parallel plates separated by $D=2.5$ mm (Fig. 1). The liquid-helium level $d=\epsilon h=1.28$ mm was chosen to eliminate the trivial density dependence due to the image charge field $\mathcal{E}_i$. The position of the helium surface was determined from the shift in the capacitance between the top and bottom plates while the cell was filled with liquid helium. The cryostat was an Oxford Instruments model 200 dilution refrigerator mounted on a vibration isolation platform which employs gimbal piston isolators. The tilt of the cell was determined from the helium levels in three identical vertical parallel plane capacitors positioned around the cell. The tilt was corrected, if necessary, by adjusting the pressures in the piston isolators. With the capacitance measurements the uncertainty in the helium level and the alignment were ∓25 μm and ∓5 mrad, respectively. The electron source was a thin tungsten filament located above the top plate behind a 200 mesh copper grid. A calibrated carbon resistor thermometer mounted on the cell was used to monitor the temperature.

To charge the surface we apply -400 V between the filament and the top plate at 1.2 K, after which the tungsten filament is briefly heated to initiate the glow discharge. Then the top plate and the guard ring voltages are ramped slowly to -50 and -55 V, respectively, to charge the surface to a density of $\simeq2.2\times10^8$ cm^{-2}, which is the maximum attainable value when $d=\epsilon h$. After the glow discharge is turned off, the system is cooled below 100 mK and the top plate and guard ring voltages are increased to -15 and to -42 V, respectively. These reference voltages were used in all density measurements discussed below.

C. Measurement of the plasmon spectrum

The density was determined from the frequencies of the rf absorption peaks in the plasmon spectra of the electron disk. Plasmon resonances were excited by transmitting an ac signal of frequency ω through a meander transmission line located underneath the electron layer. The meander line creates a longitudinal excitation field in the plane of the electrons that can be expressed as a sum of plane waves:

$$E(x,z,t)=\sum_s E_s e^{i(\omega t-k_s x)}e^{-k_s z}\ , \tag{2}$$

where E_s is the Fourier component of the electric field generated by the meander line at wave number $k_s=sk_0+\omega/v_L$, $s=0,1,2,\ldots$, and $H=2\pi/k_0$ is the period of the meanders as illustrated in Fig. 3(b). The parameters of the meander line were chosen so as to match the propagation velocity of the electromagnetic waves in the line, $v_L=cH/L\epsilon_{\rm eff}^{1/2}\sim10^8$ cm/s, to the propagation velocity of the screened plasmons in the electron layer in the density range of $(0.02-2.0)\times10^8$ cm^{-2}. Here L is the length of a meander [Fig. 3(b)] and $\epsilon_{\rm eff}$ is the effective dielectric constant for electromagnetic waves propagating above the line. The meander line was photolithographically etched from a 4-μm-thick copper film sputtered on a 25-μm-thick kapton sheet which was later glued to the bottom plate of our cell. Its impedance was 50 ∓ 1 Ω for $\omega\le2$ GHz.

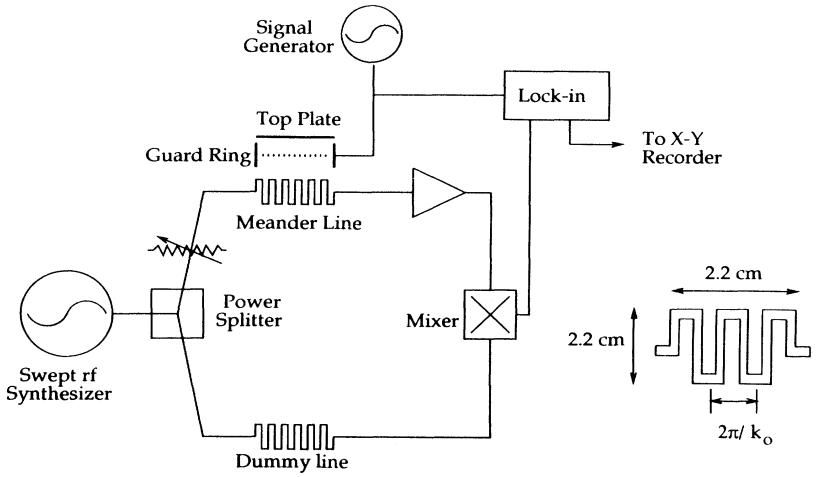

FIG. 3. The schematics of (a) the rf spectrometer, (b) the meander line. The strips of the meander line were 40 μm wide and 50 μm apart.

In Fig. 3(a) we show the schematics of the rf spectrometer. The 10-dBm output from a swept frequency synthesizer was equally divided by a power splitter between a compensating line and the meander line. A variable attenuator reduced the power level into the meander line to within a range of -40 to -60 dBm. The signal transmitted through the meander line was then amplified and compared to the signal output from the compensating line with a double balanced mixer which produces a dc output proportional to the phase difference of the two input signals. We adjusted the length of the compensating line so as to equalize the electrical path lengths of the two spectrometer arms. When rf power is absorbed by one of the plasmon modes of the electron disk, it changes the effective path length of the meander line, which gives rise to a phase shift in its output signal. This phase shift is detected by the mixer. The background signal was subtracted by locking the mixer output onto a low frequency at which the electronic density was modulated. We modulated the electronic density by applying an ac voltage of frequency 100–300 Hz and amplitude 0.1–0.5 V to the guard ring.

D. Determining the electron density

The boundary condition of vanishing radial current at the edge of the charge disk quantizes the plasmon spectrum by restricting the k vectors to a discrete sequence. By measuring the frequencies of the plasmons we can in turn deduce the plasmon dispersion relation and the electronic density. It is straightforward to calculate the spectrum of allowed k vectors for a step-function charge distribution:

$$n_0\sigma(r)=\begin{cases} n_0, & r\le R^* \\ 0, & r\ge R^* \end{cases}, \tag{3}$$

where R^* is the radius of the charge disk. The sequence of allowed wave vectors, $k_{\nu\mu}$, which determines the plasmon spectrum of the electron disk is then given by the condition $J'_\nu(k_{\nu\mu}R^*)=0$, where J'_ν is the derivative of an integral order Bessel function.[24]

The frequencies of the plasmon resonances are then found by substituting the values of the allowed wave vectors in the dispersion relation of plasmons in a two-dimensional electron liquid:

$$w^2(k)=\frac{4\pi n_0 e^2}{m}\frac{k}{\coth(kh)+\epsilon\coth(kd)}, \tag{4}$$

where we took into account the screening by the top and bottom electrodes. In the long-wavelength limit $k^{-1}\gg h,d$ the dispersion relation is linear in k: $\omega=vk$ and $v=((4\pi n_0 e^2/m)[hd/(d+\epsilon h)])^{1/2}$.

The step-function approximation of the density profile (3) is adequate for a cell with a small aspect ratio, $D/R\to 0$, but for our cell $D/R=0.2$ and the small deviations from this density profile introduce significant corrections to the plasmon wave numbers. The density distribution for $d=h$ and $D/R\ll 1$ was calculated by Glattli *et al.*,[25]

$$n_0\sigma(r)=n_0\frac{\{\sinh[(R-r-s)\pi/D]\sinh[(R+r+s)\pi/D]\}^{1/2}}{\cosh[(R-r)\pi/D]}, \tag{5}$$

where n_0 is the density at the center of the disk and s is the distance from the edge of the charge disk to the guard ring and is given by

$$\sinh^2\left[\frac{\pi s}{2D}\right]=\frac{2V_g-\mathcal{E}_c D-V_t}{2\mathcal{E}_c D}\ , \tag{6}$$

where V_g is the guard ring voltage. The total number of electrons in the disk is

$$N=n_0\int_0^{R-s}2\pi\sigma(r)r\,dr\ . \tag{7}$$

The quantized k vectors, to first order in D/R^*, are found by solving

$$k_{\nu\mu}R^*J'_\nu(k_{\nu\mu}R^*)=-\nu^2\frac{D}{\pi R^*}\cosh\left[\frac{\pi s}{D}\right]\ln\left[\tanh\left[\frac{\pi s}{D}\right]\right]\times J_\nu(k_{\nu\mu}R^*)\ , \tag{8}$$

where the effective radius of the disk is

$$R^*=\int_0^{R-s}dr/\sigma(r)\ . \tag{9}$$

After obtaining the resonance frequencies from the rf spectrum, we numerically determined the density by using (4)–(9). For an initial estimated density we calculated the radius of the disk from (6). Subsequently this value of the radius is used in (8) to evaluate $k_{\mu\nu}$, which are substituted in the dispersion relation (4) to determine the plasmon spectrum. After the calculated and the measured spectra are compared, a better estimated value for the density is obtained and the spectrum is recalculated with this new value. This process is continued until the measured and the calculated spectra are in satisfactory agreement.

E. Measurement of the electron density in the Wigner solid phase

At sufficiently low temperatures, where the electrons solidify into a Wigner crystal, the rf absorption spectra consist of a series of temperature-dependent broad peaks corresponding to coupled ripplon-phonon modes. The quality factor of these resonances is typically $Q=\omega/\Delta\omega\leq 5$, where $\omega,\Delta\omega$ are the resonance frequency and width. For $k\ll n_0^{1/2}$ the longitudinal phonon dispersion of the electron crystal is still given by Eq. (4), reflecting the fact that the electron system is nearly incompressible. On an undeformable surface this dispersion relation remains unchanged even if the electron crystal is pressed into the substrate. However, as is the case in most experiments, when the electron crystal is pressed by the external field $\mathcal{E}_p$ into the surface of a deformable substrate, such as liquid helium, it imprints a dimple lattice in it. The dimples scatter ripplons resonantly for wave vectors that are commensurate with the reciprocal-lattice vectors of the electron crystal, **G**. The resulting enhancement of the electron-ripplon interactions opens a gap in the plasmon dispersion relation whenever the plasmon frequency coincides with the ripplon frequency $\Omega_G=(\alpha/\rho)^{1/2}G^{3/2}$, where α and ρ are the surface tension and density of helium:[26]

$$\omega^2=\omega_p^2+\sum_G e^{-2W_G}\frac{ne^2\mathcal{E}_p^2}{2m\alpha}\frac{\omega^2}{\omega^2-\Omega_G^2}\ . \tag{10}$$

Here $W_G=1/4G^2\langle u^2\rangle$ is the Debye-Waller factor for the electron lattice and $\langle u^2\rangle\propto T$ is the mean-square fluctuation of the electronic position at temperature T. For frequencies $\omega\gg\Omega_G$ such that $e^{-2W_G}\ll 1$ (typically $\omega\geq 50$ MHz) the dispersion relation takes the form

$$\omega^2=\omega_p^2+\omega_0^2(t,\mathcal{E}_p)\ , \tag{11}$$

where the gap frequency $\omega_0^2(T,\mathcal{E}_p)=\sum_G e^{-2W_G}(ne^2\mathcal{E}_p^2/2m\alpha)$ corresponds to the vibration frequency of the electron in its dimple. As the gap diminishes with increasing temperature, the frequencies of the plasmon-ripplon resonances of the electron crystal decrease and the spectrum approaches that of an electron liquid.[26]

Figure 4 illustrates the temperature evolution of the rf spectrum of an electron crystal of density $n=1.5\times10^8$ cm^{-2}. We plot the rf spectra for a sequence of increasing rf power levels which can heat the electrons when applied at a resonance frequency, while not affecting directly the

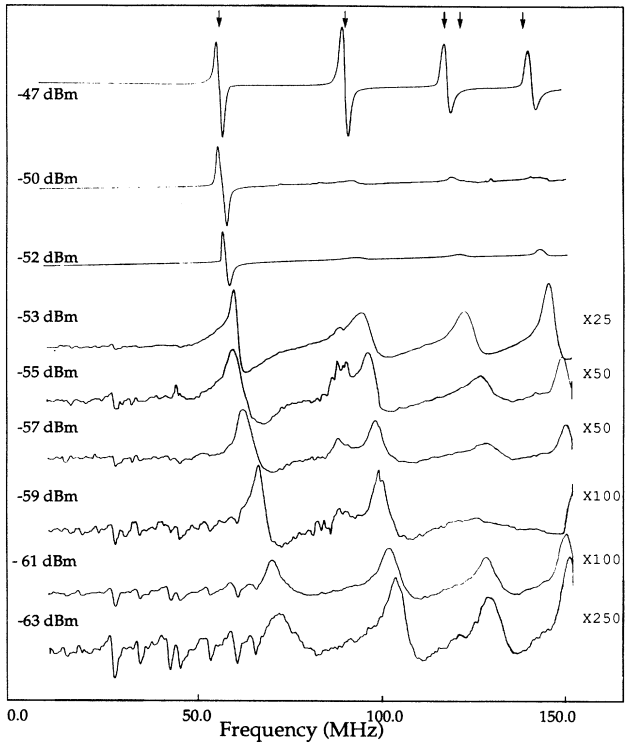

FIG. 4. The rf power dependence of the spectra at $T=0.04$ K and $n_0=1.5\times10^8$ cm^{-2} when the 7-dBm output of the swept frequency synthesizer was fed into the meander line through an attenuator. The power levels were marked on the graph. The arrows indicate the positions of the calculated plasmon resonances.

helium substrate which is kept at a temperature of $T=0.040$ K. We note that as the rf power increases the resonance frequencies drift downwards and the amplitude grows nonlinearly, indicating an increase in the electronic temperature. There is a critical power level where the absorption peaks suddenly become very narrow and above which the resonance frequencies remain fixed. The frequencies of these resonances are identical to those one would obtain for uncoupled plasmons. Their narrowing and frequency downshift imply that the electron crystal melts during the passage through the resonances if the rf power level exceeds the critical power.

These narrow and temperature-independent resonances give a more accurate measurement of the electronic density than the broad phonon-ripplon-coupled spectrum. In order to melt the solid while keeping the liquid helium at 40 mK, we increased the rf power and reduced the thermal coupling of the electrons to the cold helium surface bath by decreasing the pressing field. The top plate voltage $V_t=-15$ V and rf power into the meander line, ~ -50 dBm, were chosen so that in the process of recording the spectra there is no measurable loss of electrons. The lifetime of the electrons under these conditions was virtually infinite, $\sim 10^7$ s. This procedure for the density determination, while giving the highest possible accuracy in the density measurement, does not, as will be discussed below, affect the tunneling rates.

Equation (8) for the allowed wave vectors is accurate for small ν while the sensitivity of the resonance to the electron density is better for high ν peaks. For all the density measurements we used the $\nu=2$, $\mu=1$ peak, the second-lowest frequency peak in Fig. 4, because of its good coupling to the meander line while at the same time it presented a good compromise between the sensitivity to the density and the accuracy of the dispersion relation. The uncertainty in the absolute value of the density was $\mp 5\%$ but the accuracy in the relative density measurements was much better, $\sim 0.01\%$. We cross checked our density measurement with the density determined from the ripplon-plasmon spectra in the solid phase without overdriving the resonances and from the liquid-solid transition temperature at which the ripplon-plasmon and transverse phonon spectra first appear. The densities determined with all three methods were in good agreement.

F. Measurement of tunneling rates

To initiate measurable escape rates we applied a voltage pulse which changed the top plate voltage from -15 V to a larger (positive) value V_t for a finite time interval Δt. During the pulse the rf power and the modulation voltage were turned off to eliminate any possible escape due to heating. Subsequently the top plate voltage was brought back to -15 V where the number of electrons lost was determined by comparing the rf spectra before and after the pulse. The pulse duration, $\Delta t \sim 100$ μs to 50 s, was adapted to the escape rates and was chosen to be short enough so that no more than a few percent of the electrons were lost in a single pulse. The rise time of the pulse ~ 30 μs was chosen so as not to induce further escape arising from transient heating. By repeated applications of pulses at a fixed amplitude V_t, we measured the time evolution of the density n_0. The tunneling rate $W(n)=[N(t)-N(t+\Delta t)]/N(t)\Delta t$ was determined from the charge distribution (5) by evaluating the number of electrons $N(t)$ at the beginning and at the end of the pulse. We then used Eqs. (5)–(7) to calculate the electron density during the pulse from the known values of the top plate and guard ring voltages and the total number of electrons, $N(t)$ and $N(t+\Delta t)$, at the beginning and the end of the pulse. Assuming that during the rise and fall of the pulse no electrons were lost, we assigned the average density during the pulse $n=[n(t)+n(t+\Delta t)]/2$ to the escape rate $W(n)$.

We studied the effect of switching the top plate voltage on the escape rates by measuring the time evolution of the density with different pulse durations in the range 150 μs–20 min. By varying the number of pulses as much as four orders of magnitude, while keeping constant the total time the electrons were exposed to a given barrier in between two density measurements, we ascertained that changing the top plate voltage with a rise time of 30 μs or slower did not cause any detectable electron loss below a critical density discussed below. When the rise time of the pulses was further decreased to ~ 1 μs, the rates started increasing precipitously at low densities when the lowest plasmon absorption frequency became comparable to the frequency introduced by the transient voltages on the top plate. We increased the rise time until there was no measurable rise-time dependence of the escape rates. To check the effects of electrical noise which may reach the meander line through coaxial cables, we lowered the barrier and kept it low while feeding rf power into the meander line at a level comparable to that used for recording the plasmon spectra. No extra loss of electrons was detected for off-resonance frequencies. We repeated some of the measurements with different guard ring voltages and found no detectable dependence of the rates on these values.

IV. RESULTS AND DISCUSSION

We measured the escape rates as a function of density, temperature, and external field. The measurable rates span 11 orders of magnitude over a temperature and density range of 35–450 mK and $(0.02-2.2)\times 10^8$ cm^{-2}. The top plate voltage was varied in the range $V_t=+10$ to -15 V, corresponding to an external field in the range $\mathcal{E}_p=-40$ to $+60$ V/cm. The external fields applied in these experiments are much smaller than both the atomic unit of electric field for surface-state electrons, 1727 V/cm, and the static field ionization limit ~ 200 V/cm. Typical magnitudes of the experimental parameters for an electron density of $n=1.0\times 10^8$ cm^{-2} are $\mathcal{E}_c=-90$ V/cm for the field of the uniform electron sheet and $r_0=1.4/\sqrt{n\pi}=0.8$ μm for the correlation hole radius.

In Fig. 5, we plot the escape rates W at 40 ∓ 5 mK as a function of density for a series of top plate voltages ranging from 9 to -15 V. The data can be separated into three different regions where W exhibits qualitatively different behavior as a function of density, external field, and pulse duration. In region A, where $W>5\times 10^{-4}$ s^{-1}

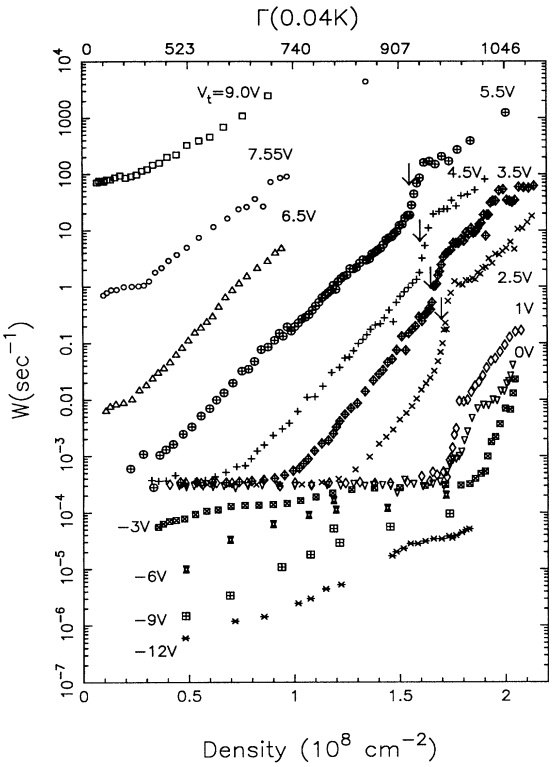

FIG. 5. The density dependence of the escape rates W at 40 ∓ 5 mK for a series of top plate voltages V_t. The vertical arrows indicate the positions of the critical densities $n_c(V_t)$ at which the escape process becomes nonlinear. On the upper scale we show the values of Γ for $T=0.04$ K.

and the density is less than a critical density $n_c(V_t)$, indicated by vertical arrows, the rates depend strongly on density and external field but are independent of the pulse length Δt. Below we show that the escape in this regime can be attributed to tunneling. In the region where $W<5.0\times10^{-4}$, referred to as region B, the rates depend weakly on density and external field but are independent of temperature. In region C, defined by $n>n_c(V_t)$, the rates depend strongly on the pulse duration, indicating a nonlinear process or an instability.

A. Region A — the tunneling regime

In region A, where the measured rates increase exponentially with density, we compare our results to calculated tunneling rates through the potential

$$U(z)=\begin{cases}-\dfrac{eQ}{z+\beta}+e(\mathcal{E}_p+\mathcal{E}_i)z+e\mathcal{E}_c\dfrac{(z-z_0)^2}{2r_0}, & z-z_0\le r_0\\ -\dfrac{eQ}{z+\beta}+e(\mathcal{E}_p+\mathcal{E}_i)z+e\mathcal{E}_c\left[z-z_0-\dfrac{r_0}{2}\right], & \\ V_0, \quad z<0\ . & z-z_0\ge r_0\end{cases}\tag{12}$$

In the zero density limit where $\mathcal{E}_c=0$, and for $\beta=0$ and $V_0=\infty$ this problem reduces to that of a one-dimensional hydrogen atom in an externally applied field. The values $\beta=1.04$ Å and $V_0=1$ eV represent corrections to the usual image potential description of the electron-helium interaction raising from the finite size of the helium-vacuum interface and the finite barrier for penetration into the helium. This value of β is chosen to fit the resonance frequencies obtained in microwave absorption measurements.[22] The second term in the potential arises from the externally applied field and the image in the metallic plates. The effects of correlations with the electrons remaining in the layer are contained in the third term. This is the CHM potential[5] modified to take into account the fact that the electron layer is located at a finite distance $z_0=\langle z\rangle=114$ Å above the helium.[27] By expanding this term about z_0 we note that the quadratic term is identical to the CHM potential used in Ref. 5, the linear term is equivalent to an additional pressing field $-(z_0/r_0)\mathcal{E}_c\le-0.03\mathcal{E}_c$ and the constant $z_0^2/2r_0\mathcal{E}_c$ gives a small (0.01%) correction to the resonance energy. By substituting $z'=z+\beta$ and by redefining the resonance energy and the pressing field to include these corrections the problem reduces to the one solved in Ref. 5. We obtained the binding energy E_B and the tunneling rates from the complex energies of the metastable state solutions of the Schrödinger equation by using the Breit-Wigner technique developed in Ref. 5. The barrier width Δz was then determined from the distance between the turning points for the calculated E_B.

We also calculated the tunneling rates in this regime from the WKB approximation: $W=W_0e^{-\gamma}$ where

$$\gamma=2/\hbar\int_{z_1}^{z_2}\sqrt{2m\,[E_B-U(z)]}\,dz$$

is the numerically calculated WKB exponent in the

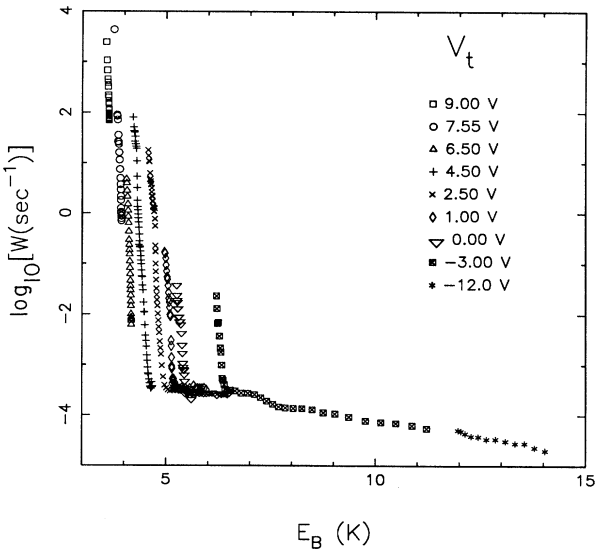

FIG. 6. The escape rates of Fig. 5 plotted as a function of barrier height calculated from the correlation hole potential (12).

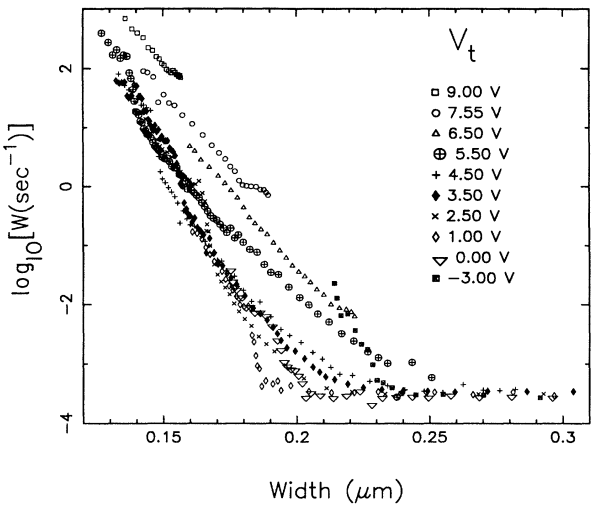

FIG. 7. The escape rates of Fig. 5 plotted against the barrier width calculated from the correlation hole potential (12).

CHM. We found that the WKB exponent is in good agreement with that calculated with the Breit-Wigner technique. The advantage of the latter is that it also gives an accurate value for the prefactor W_0. The value of E_B used in the WKB calculation can be approximated (when $V_t > 0$) by

$$E_B \simeq 0.523 + 3|\mathcal{E}_p|/2 + 3|\mathcal{E}_c|/2r_0 - \begin{cases} 2\sqrt{|\mathcal{E}_p|}, & |\mathcal{E}_c| \ll |\mathcal{E}_p| \\ 3(|\mathcal{E}_c|/r_0)^{1/3}/2, & |\mathcal{E}_p| \ll |\mathcal{E}_c| \end{cases} \quad (13)$$

and the barrier width

$$\Delta Z \simeq (r_0|\mathcal{E}_p|/|\mathcal{E}_c|)[(1+|\mathcal{E}_c|/r_0\mathcal{E}_p^2)^{1/2}-1]-2 . \quad (14)$$

Here all quantities are expressed in scaled atomic units: energy = 15.2 K, length = 76.1 Å, and electric field = 1727.2 V/cm. In our experiment $20 < \Delta Z < 80$, $0.2 < E_B < 1$, and $70 < r_0 < 700$. As a first check on the escape mechanism in region A we replot in Figs. 6 and 7 the data of Fig. 5 as a function of E_B and ΔZ. We observe that in region A, for $E_B \leq 6.5$ K, the rates drop exponentially with increasing barrier height and width, as expected of tunneling. Below $T = 200$ mK, the rates are temperature independent, again as expected of tunneling. The temperature dependence of the escape rates is further discussed in Sec. IV.

Next we compare the measured rates with the calculated tunneling rates. The tunneling rates are exponentially sensitive to the cell height, the helium level, the density, and the voltage difference between the plates. Therefore, a comparison between the calculated and measured rates requires precise knowledge of these quantities. The accuracy of the capacitively measured helium level is 1% and the relative density measurement is accurate to within 0.01%. The dimensions of the cell parts are measured to within ± 12 μm. After assembly, the separation between the top and bottom plates was calculated from the total cell height and the dimensions of the individual parts to be 2.55 ± 0.05 mm at room temperature. Capacitance measurements indicate that upon cooling the cell contracts by 2% resulting in a cold cell height of 2.5 ± 0.05 mm. Finally, the externally applied voltage was measured to within ± 5 mV. An additional uncertainty in this experiment stems from the fact that the actual voltage difference between the top and bottom plates can differ from the externally applied voltage. This happens in the presence of a surface dipole layer which can form due to the work-function difference between the plates or as a result of adsorbed species and trapped charges. As the cell is cooled adsorption on its walls could further change the contact potential. We attempted to measure the contact potential in the cold cell by three different methods.

(1) Measurement of the equilibrium density as a function of applied pressing voltage. After charging the surface to a voltage V_t at $T = 1.2$ K, we determined the density from the rf spectrum recorded after cooling to base temperature. The contact potential was then calculated from the equilibrium condition $2\pi ne = -(\epsilon+1)(V_t + V_c)/2D$. The accuracy of this method is limited by the precision with which the absolute value of the density can be determined. This method gave a con-

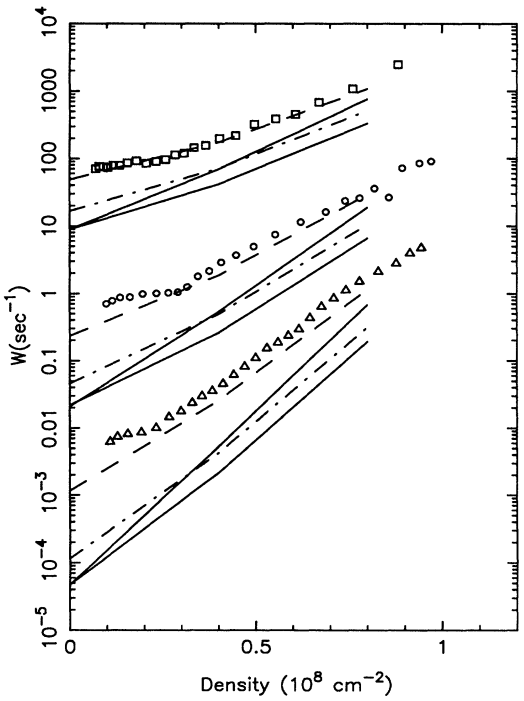

FIG. 8. Tunneling rates calculated in the correlation hole model potential (12): (lower solid line) helium level is at the electrical middle, $d = \epsilon h = 1.28$ mm, and cell height $D = 0.250$ cm, (upper solid line) $d = 1.305$ mm and $D = 0.250$ cm, (dot-dashed line) $d = 1.28$ mm and $D = 0.245$ cm, (dashed line) $d = 1.28$ mm, $D = 0.25$ cm and a pulling contact potential of $+0.5$ V. The rates are calculated for $n = 0$, 0.4, and 0.8×10^8 cm^{-2}. The lines are drawn to guide the eye. Top plate voltages are (□) 9.0 V, (○) 7.55 V, and (△) 6.5 V.

tact potential which was in the range 1–2 V.

(2) After charging the helium to a given value of V_t we reduced the guard ring voltage until a loss of electrons was first observed. This was interpreted as a sign that the electron disk has expanded and made contact with the guard ring. The values of V_t and V_g corresponding to this situation are then used in Eq. (6) to determine the actual potential difference across the cell. The accuracy of this method depends on the precision of the density measurement. The value of the contact potential will also depend on whether there is a contact potential between the top plate and the guard ring. By assuming no contact potential between these two electrodes, this method gave $2 \leq V_c \leq 3$ V.

(3) We measured the current to the bottom plate as a function of top plate voltage while injecting charges from the filament discharge into the region between the top and bottom plates. When the temperature was sufficiently high, $T \geq 1.2$ K, the injected charges would thermalize well before reaching the bottom plate and give rise to a drift current caused by the electric field between the plates. Measuring the top plate voltage where the current was zero would then be equivalent to measuring the voltage difference between the bottom and top plate, provided there is no charge accumulation between them. By using this method we found $1 \leq V_c \leq 2$ V.

In spite of the large scatter in the data there was an internal consistency between the results for V_c: $V_c > 0$ for all the runs in which electrons were introduced in the cell, indicating a pulling field, and changed sign only when the bottom plate was bombarded with positive ions. In one of the runs in which we changed the experimental procedures significantly, the tunneling rates were markedly slower than in the others. At the same time we noted a 1-V *decrease* in V_c (as measured by the last two methods but not with the first) which was consistent with a slow down of the escape rates due to an increase in the barrier size. We speculate that this change in V_c was caused by a new configuratoin of trapped charges. The tunneling measurements were repeated numerous times over a two-year period. Throughout these experiments, for similar experimental conditions, the measured rates were reproducible to within a factor of 2. We did not observe sharp changes in the rates unless a large number of electrons or positive ions were injected into the cell or the procedure of charging and cooling was significantly modified. This indicates that the charge distribution on surfaces inside the cell does not vary arbitrarily during the experiments or between runs.

In Fig. 8 we illustrate the sensitivity of the calculated rates to the uncertainty in the measured experimental pa-

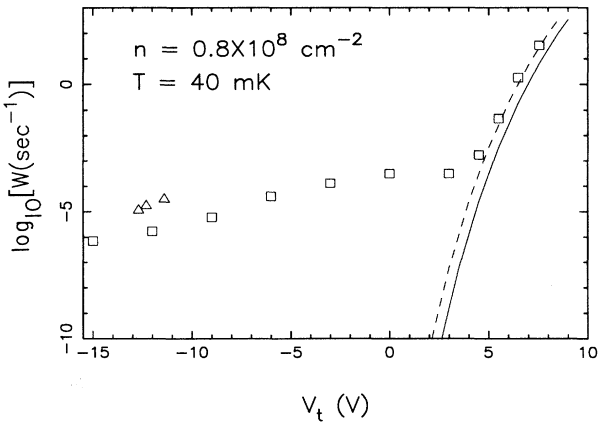

FIG. 9. The escape rates as a function of top plate voltage V_t at the density $n = 0.8 \times 10^8$ cm^{-2} and $T = 40 \mp 5$ mK. The squares represent the data from Fig. 5 and the solid line shows the calculated rates from the correlation hole model. The triangles are the rates reported in Ref. 7. The top plate voltages of Ref. 7 were scaled so as to give the same field value for our cell. Dashed line shows the rates when the contact potential $V_c = 0.5$ V.

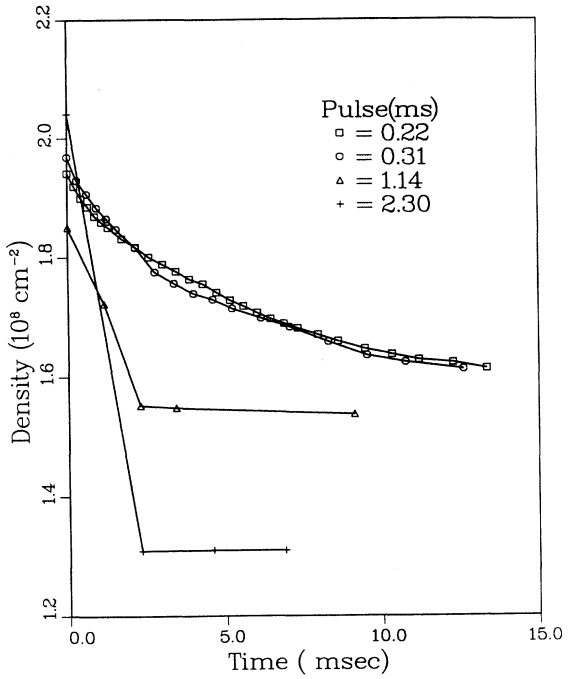

FIG. 10. The time evolution of the density at $T = 0.04$ K measured by different pulse durations above the critical density at $V_t = 4.5$ V. The lines were drawn to guide the eye. The pulse durations are marked on the graph.

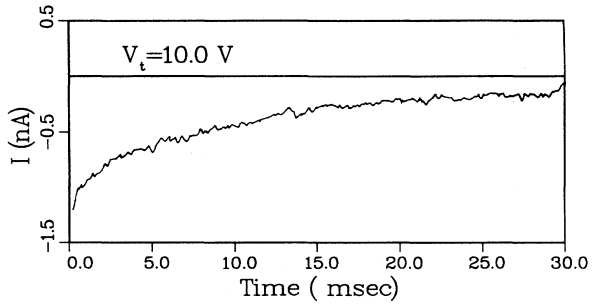

FIG. 11. The time dependence of the tunneling current in region A for an initial density of 1.2×10^8 cm^{-2} and top plate voltage $V_t = 10.0$ V. In this experiment the helium level was $d = 0.117$ cm.

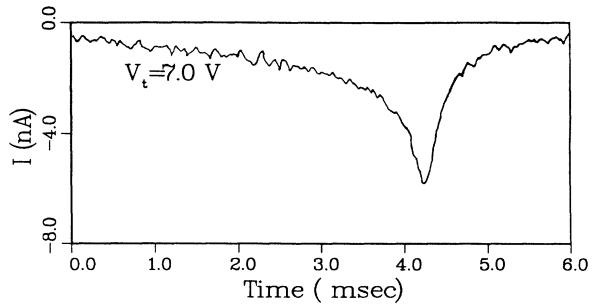

FIG. 12. The time dependence of the tunneling current in region C. The initial density and top plate voltage were 2.3×10^{8} cm^{-2} and 7.0 V. The density at the position of the peak is equal to the critical density $\approx1.3\times10^{8}$ cm^{-2}. In this experiment the helium level was $d=0.117$ cm. The current measured in a subsequent pulse of $V_t=10.0$ V is shown in Fig. 11.

rameters: ±50 μm in the cell height, ±25 μm in the helium level, and the contact potential. These are compared to the measured escape rates for three runs with different applied voltages. We note that if we assume $V_c=0$ the measured rates would be almost one order of magntiude faster than the calculated ones and this gap cannot be closed by adjusting the values of the cell height or the helium level within their range of uncertainty. However, by assuming a contact potential of $+0.5$ V the calculated rates align neatly with the measured ones for all the data. This value of V_c is somewhat below the range of the measured values described above. It should be noted, however, that an equally good agreement between the data and the calculated rates[5] was obtained by assuming $\beta=0$, $V_0=\infty$, $V_c=0$, and $D=2.50$ mm and a helium level of $d=1.255$ mm.

We conclude that the data in region A are consistent with the tunneling mechanism. However, although the density dependence of the tunneling rates is an accurate measure of the contribution of correlations to the potential, the uncertainties in the measured parameters do not allow a reliable determination of the details of the potential near the helium surface.

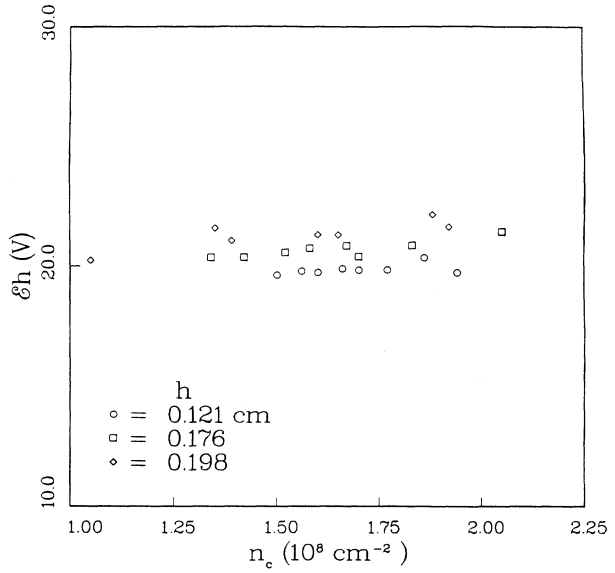

FIG. 13. The critical density plotted against the voltage difference between the electron layer and the top plate for three different helium levels, $d=D-h$.

B. Region B — the limiting rates

In region B, the escape rates $W\leq5\times10^{-4}$ s^{-1} and depend very weakly on density and external field. For pulling fields, $V_t>0$, and low densities all the data converge to a single value of the escape rate. When the direction of the external field is reversed from pulling to pressing (from a positive V_t to a negative value) the rates become weakly density dependent again.

To gain insight into the escape mechanism in this regime we replot in Fig. 9 a slice of the data in Fig. 5 at fixed density, $n=0.8\times10^{8}$ cm^{-2}, as a function of the top plate voltage V_t. We note that the calculated rates follow closely the measured ones for $V_t\geq4$ V, region A, and break away sharply at smaller voltages where the limiting rates take over. We also show the temperature-independent rates reported in Ref. 7, which are clearly situated in region B. The reasonable agreement between the two sets of measurements suggests that the rates in this region may not be experimental artifacts. As shown in Figs. 6 and 7, when the barrier becomes larger, $E_B\geq6.5$ K and wider $\Delta Z\geq0.5r_0$, the escape rates become independent of the barrier width and depend only on its height. The exponential barrier height dependence of the rates in region B suggests an activated escape mechanism with an effective temperature of ~3.5 K.

The data strongly suggest that tunneling might not be the primary escape mechanism in region B, so that with increasing barrier size a new escape mechanism becomes dominant and puts a lower limit on the observable tunneling rates. It is not clear what the origin of this escape is and whether the interpretation of the slope of Fig. 6 in terms of a temperature is justified since, to our knowledge, nothing in our experiment is this hot. So far we have ruled out vibrations or a tilt of the helium surface as the source of the limiting rates. Another possibility is that the electrons are weakly coupled to a photon reservoir that may form due to radiation that is guided into the cell through the electrical leads. To reduce the amount of radiation into the cell we have inserted microwave filters into all the leads. The filters (100-dB attenuation at 5 GHz) were thermally grounded at the mixing chamber. The installation of the filters did not introduce a measurable change in the limiting rates. As for the escape rates in region A, we did observe a consistent decrease in the rates for $n\rightarrow0$ limit, but this rate reduction which was at most by a factor of 2, did not exceed the measurement error.

C. Region C — the instability

In region C, located to the right of the vertical arrows in Fig. 5, the escape rates become very nonlinear in the pulse duration Δt. In Fig. 10 we present the time evolution of the density as measured with different pulse lengths for $V_t=4.5$ V. For $\Delta t\leq200$ μs, the decay of the density is not very sensitive to the pulse duration. As Δt increases the rates became successively more sensitive to

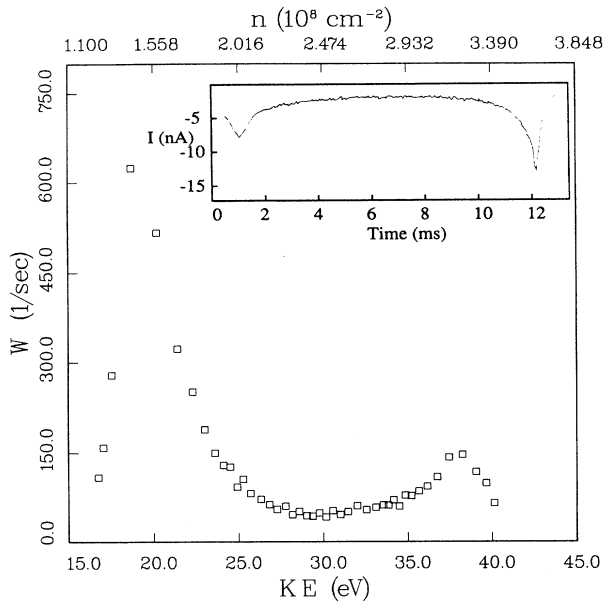

FIG. 14. The impact energy dependence of the rates above n_c in the energy range 15–45 eV. The slope of the 20-eV peak on the low-energy side is mostly due to the response time of the current amplifier. In this experiment the helium level d was 0.117 cm. In the inset we show the current which was integrated to obtain the impact energy and density.

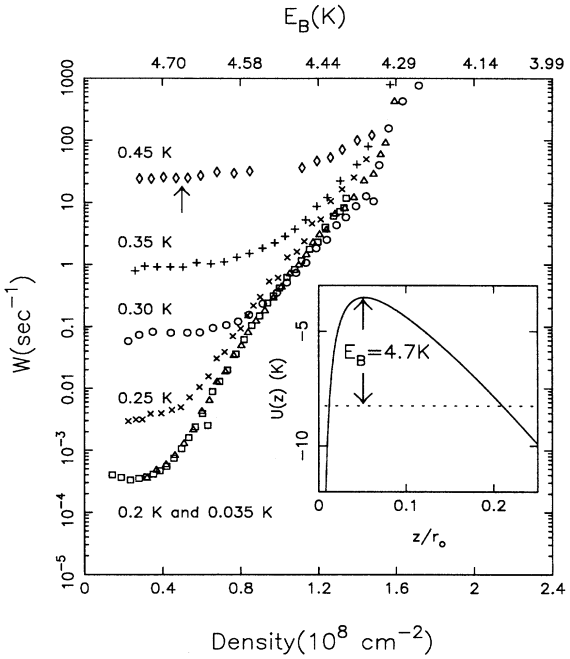

FIG. 15. The temperature dependence of the escape rates for the pulling field of $V_t = 5.5$ V. The inset illustrates the correlation hole barrier and the resonance energy for $V_t = 5.5$ V and $n = 0.4 \times 10^8$ cm^{-2}. The arrow on the $T = 0.45$ K data indicates the density corresponding to $\Gamma = 47$ where an instability was reported in Ref. 14.

the pulse duration and for $\Delta t \geq 0.5$ ms a large fraction of the electrons is lost before the system stabilizes itself again at a density $n < n_c(V_t)$. The data points in region C that are depicted in Fig. 5 were measured with very short pulses, $\sim 150\ \mu$s.

A better understanding of the instability in region C was gained by measuring the tunneling current. A current amplifier was connected between the meander line and the electrical ground to detect the current induced by the escaping electrons. Figure 11 shows the typical time evolution of the tunneling current in region A, where it decays exponentially and no instability develops. To study the time evolution of the current in region C, it was convenient to charge the surface to a higher density, $n_c < n \leq 4 \times 10^8$ cm^{-2}, which was possible to do by slightly reducing the helium level to $d = 0.116$ cm. The maximum density 2×10^9 cm^{-2} can be attained for $d < 0.10$ cm. In Fig. 12, we show a typical trace of the tunneling current in region C obtained during a 6-ms pulse of $V_t = 7.0$ V for an initial density of 2.3×10^8 cm^{-2}, well above the critical density. At the beginning of the pulse the current is almost zero, but grows exponentially in time until it peaks at the critical density and subsequently decays exponentially.

For the helium level used in the data of Fig. 5, $d = 0.128$ cm, we found that the locus of critical densities separating regions A and C is determined by the empirical condition $\mathcal{E} = (\mathcal{E}_p + \mathcal{E}_c + \mathcal{E}_i) = -164$ V/cm, where $\mathcal{E}$ is the total field above the electron layer, or equivalently by $U = h\mathcal{E} = 20 \pm 1$ V, where U is the potential difference between the electron layer and the top plate. In order to resolve whether the total field or the potential difference is the relevant parameter, we measured the critical densities with three different helium levels. The results, plotted in Fig. 13, show that with all three helium levels the instability starts at the same potential difference of $U = 20 \pm 1$ V, indicating that the onset of the instability is associated with the kinetic energy of the escaping electrons when they impact the top plate. This value of the threshold kinetic energy is very close to the lowest two excitation energies of the helium atom: 19.8 and 20.6 eV for the first excited orthohelium state $1s2s\,^3S$ and parahelium state $1s2s\,^1S$, respectively, while the ionization threshold is at 24.5 eV. This suggests that impact excitations of the atoms in the superfluid helium film coating the top plate are responsible for triggering the instability.

This is better illustrated in Fig. 14 where we plot the tunneling rate for an initial density of 3.5×10^8 cm^{-2} as a function of the impact energy in the range 0–45 eV. We observe two peaks and a relatively flat region between them. The first peak occurs at 19.6 eV, the energy necessary to excite one helium atom, while the second at 39 eV suggests a process involving the excitation of two helium atoms.

The details of the connection between the instability and the excited helium atoms still need to be clarified, but our experiments suggest they are closely linked. The

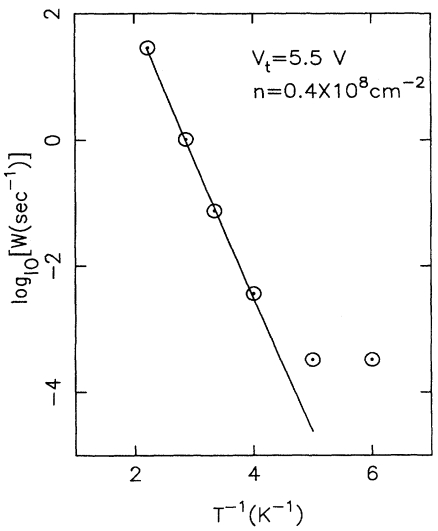

FIG. 16. The escape rate vs inverse temperature. The circles represent a slice of the data in Fig. 15 at fixed density $n=0.4\times10^8$ cm^{-2}. The solid line is a two-parameter fit to the calculated thermally activated rates, with $E_B=4.4\pm0.1$ K and $C=0.071$.

thickness t of the helium film coating the top plate is given by $t=t_0/h^{1/3}$, where $h=0.12$ cm is the separation of the top plate and the helium surface, and $t_0\simeq350$ Å/cm$^{-1/3}$ for metal surfaces.[28] Certainly the helium film covering the top plate is sufficiently thick, $\simeq700$ Å, so as to result in an ionization or excitation probability of roughly 1 (Ref. 29) when hit by an electron with the appropriate kinetic energy. The 20-eV photons emitted by these excited helium atoms can interact with the surface-state electrons either directly or via excitations of the liquid helium. Alternatively they may produce photoemitted electrons on the cell walls which may lead to an avalanche of escaping electrons. Since $\mathcal{E}_p$ is kept constant during the experiment, it is $\mathcal{E}_c=-2\pi ne$ which determines the impact energy of U. As the electrons escape, their density decreases and with it the energy they transfer to the helium atoms. When the density has decreased below the critical value where the impact energy of the escaping electrons is less than the excitation threshold of the helium atom, this process stops. This explanation of the instability is also consistent with the fact that the critical densities are temperature independent, as discussed below.

Three different types of instabilities have been reported for the SSE at the helium-vacuum interface. The instability we have observed in region C is unlike any of those reported so far.

The electrohydrodynamic instability caused by the softening of the ripplon-plasmon modes puts an upper limit of 2×10^9 cm^{-1} on the density that can be sustained on a bulk helium substrate. Beyond this density the electrostatic pressure exerted by the electrons on the helium surface when an external pressing field is applied can no longer be restored by the surface tension, and the surface collapses.[30] The instability in region C is of different origin since it occurs even at zero electrostatic pressure.

In Ref. 31 another stability boundary has been reported which was attributed to interactions with electrons in thermally populated excited states. However, in region C of our experiments the instability is independent of temperature and the potential barrier can support only one

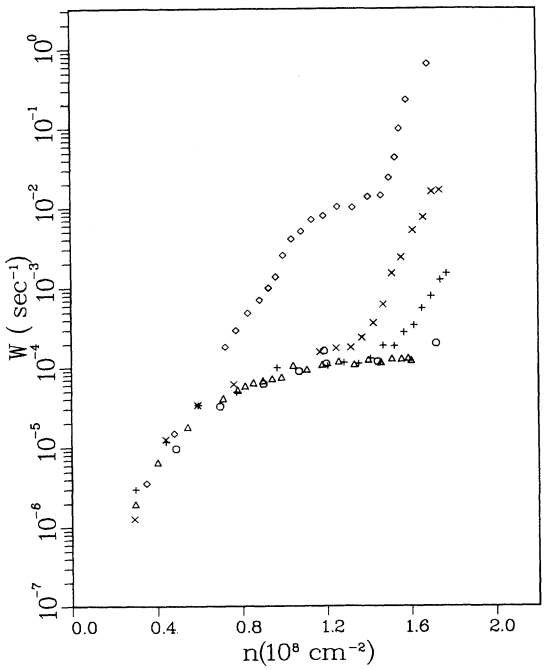

FIG. 17. The density dependence of the escape rates for $V_t=-6.0$ V at a series of temperatures: ◇, 0.45 K; ×, 0.35 K; +, 0.30 K; ○, 0.20 K; △, 0.04 K.

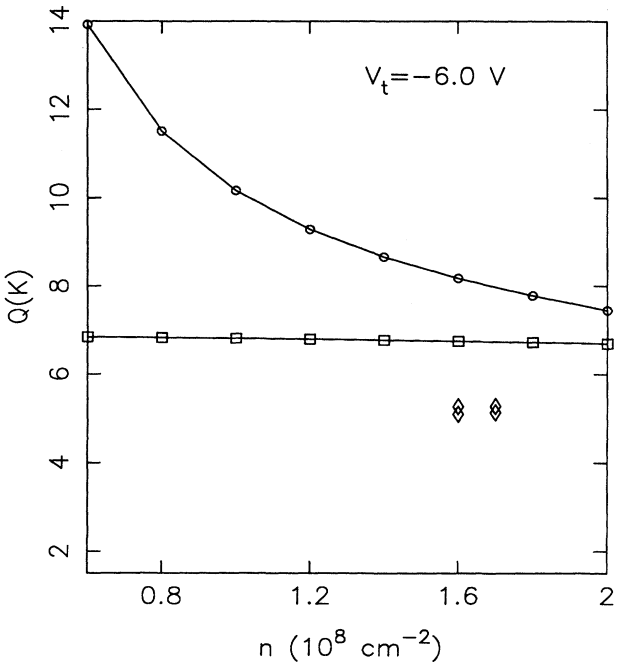

FIG. 18. The activation energies (□) to the first excited state and (○) to the top of the barrier calculated from the correlation hole potential (12). We also show (◇) the values obtained from the data of Fig. 17 at 0.450 K and 0.350. The lines are drawn to guide the eye.

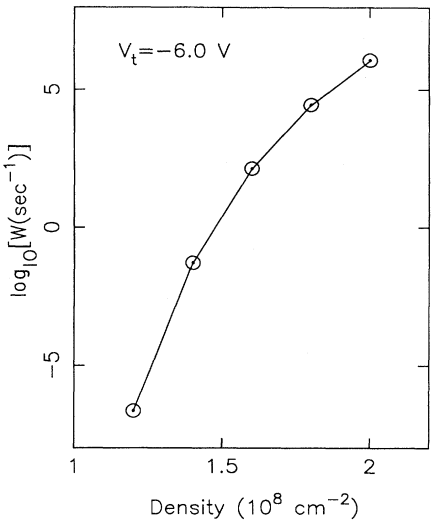

FIG. 19. The calculated tunneling rates from the first excited state of the correlation hole potential at $V_t=-6.0$ V. They were obtained for five densities and the lines between them were drawn as a guide to eye.

quasibound state, which rules out this explanation. We did not study the instability reported in Ref. 31 since it was outside the density and temperature range of our experiments.

Buntar *et al.*[14] reported a precipitous increase in the escape rates when the classical ordering parameter $\Gamma=47$. They attributed this instability to a transition between a glassy phase and an electron gas. In Fig. 15, where the escape rates were plotted at $T=0.45$ K, we have indicated by an arrow the position where $\Gamma=47$. In the vicinity of this point the rates vary monotonically and do not seem to exhibit any instability.

D. Thermal activation

1. Thermal activation in region A

In Fig. 15 we plot the temperature dependence of the escape rates in region A for $V_t=5.5$ V. Below 200 mK the data are independent of the temperature, as expected of tunneling. As the temperature is raised, the low-density portion of the escape rates becomes temperature dependent and peels off the steep tunneling rates at successively higher values of density.

In Fig. 16, we plot the escape rates as a function of inverse temperature at a density of $n=0.4\times10^8$ cm^{-2}. Above $T=0.2$ K we observe activated-type behavior. Since the escaping electrons are coupled to ripplons and helium gas atoms, the activated rates should be of the form $(P_R+P_G)\exp(-E_B/kT)$ where P_R and P_G are electron-ripplon and electron-gas collision rates, respectively. But in this experiment, where $T<0.5$ K, the helium vapor pressure is negligible and therefore it is sufficient to consider electron-ripplon scattering alone. The solid line in Fig. 16 is a two-parameter fit to the theoretical expression for this process:[32]

$$W=C\left[\frac{m}{\hbar^3\alpha}\right]T^2E_B\left[1+\frac{3k_BT}{E_B}\right]\exp\left[-\frac{E_B}{k_BT}\right]. \quad (15)$$

Here α is the helium surface tension and $C=0.354$ is a prefactor obtained from a first-principle calculation of P_R in the uncorrelated limit, $r_0=0$. The best fit for the barrier height $E_B=4.4\mp0.1$ K is lower than the value calculated from the modified CHM potential in the absence of a contact potential: $E_B=4.7$ K. Assuming a contact potential correction of $V_c=+0.5$ V (the value of V_c which brings the calculated tunneling rates in agreement with the measured ones), the calculated barrier height becomes 4.57 K.

We note that the temperature-dependent escape rates are practically constant in density. This is not surprising since the height of the CHM barrier indicated on the upper horizontal scale is almost density independent in this regime. Thus, we conclude that all the aspects of the temperature-dependent data studied in region A are consistent with thermally activated escape.

2. Thermal activation in region B

For all the barriers in region A the potential has only one metastable state. This simplifies the interpretation of the escape data considerably since the absence of a sequence of metastable states ensures that escape by a more complex multistep process, such as thermally assisted tunneling, cannot occur.

In Fig. 17, we plot the temperature dependence of escape rates for a pressing field, $V_t=-6.0$ V. For $T>0.2$ K they increase with temperature and exhibit a complicated density dependence. Regardless of the temperature, all curves overlap at low densities. Part of the complex behavior in this regime might stem from the fact that the barrier is higher than in region A and has excited states. We illustrate this in Fig. 18, where we plot in the excitation energies to the top of the barrier and to the first excited state in the CHM. On the same graph, we also indicate the experimental activation energy calculated from the expression

$$Q(n)=-\frac{\ln\{(T_2^2/T_1^2)[W_1(n)/W_2(n)]\}}{(1/T_1-1/T_2)} \quad (16)$$

by using the $T_1=0.350$ K and $T_2=0.450$ K curves of Fig. 17 at the two densities $n=1.6$ and 1.7×10^8 cm^{-2}. For these densities $Q(n)$ is well below the excitation energy to the top of the barrier and roughly 1 K below the activation energy to the first excited state. At lower densities the thermally activated rates reach the limiting rates at $T=0.350$ K and the data can no longer be used to calculate $Q(n)$.

At 0.450 K, the rates mostly lie above the limiting rates and exhibit two different types of density dependence separated by a plateau. At high densities where the barrier height is expected to be almost constant, the rates increase rapidly with the density, indicating that the density dependence is coming through another process. A likely mechanism for the enhanced escape rates is

thermally assisted tunneling, whereby electrons tunnel from a thermally populated excited state. As pointed out by Yücel and Andrei,[5] the tunneling rates increase much faster with density than the thermally activated rates. Consequently, as the density increases, tunneling from the excited states will eventually become more probable than thermal activation to the top of the barrier. Therefore, at high densities and elevated temperatures, the escape rates are expected to become strongly density dependent, as verified by our data.

At low densities, however, we expect thermal excitation to the top of the barrier to be the dominant escape mechanism. As illustrated in Fig. 19, the tunneling rates from the first excited state as calculated in the CHM are strongly density dependent. For $n < 1.4 \times 10^8$ cm^{-2}, they become negligibly small, indicating that thermally assisted tunneling does not play a role in the low-density regime. Consequently the plateau region in Fig. 17 can be attributed to thermal activation to the top of the barrier whose height in this regime is almost independent of density.

V. TUNNELING AND THE LIQUID-SOLID TRANSITION

Most of the data in Fig. 5 represent escape out of the Wigner crystal phase as can be seen from the values of the classical ordering parameter Γ marked on the upper scale. As the density decreases the crystal melts into a liquid at $\Gamma = 127 \pm 3$. But the escape rates vary smoothly through the transition indicating that the tunneling process is insensitive to the long-range order in the electron layer. This might not come as a complete surprise since throughout our experiments the barrier width is smaller than the interelectronic spacing, $\Delta Z < 0.5 r_0$, so the escaping electron interacts primarily with its nearest neighbors while it tunnels. On this short length scale the liquid and solid phases are indistinguishable.

VI. CONCLUSIONS

We have observed the effects of electron-electron correlations on the tunneling of electrons bound to a liquid-helium surface. In the relatively low-density regime studied in this work we did not observe the dynamical response of the electron lattice to the tunneling. Neither did we observe any structure in the density dependence of the rates at the liquid-solid phase transition. These effects are expected to be significant when the barrier width is comparable to the interelectronic spacing, and when the response time of the electron layer is of the order of the tunneling time. We estimate that in our system this should occur for densities $n \geq 10^9$ cm^{-2}. Although we have not yet been able to accurately measure tunneling rates for such high densities, we demonstrated the feasibility of a new generation of experiments which could reveal the many-body and time-dependent aspects of tunneling.

ACKNOWLEDGMENTS

This work was supported by NSF Grant No. DMR-90-24964. We would like to thank A. Ruckenstein, Y. Vil'k, and F. I. B. Williams for useful discussions and C. Chaleil-Hulier, W. Henderson, and J. Verrier for technical support.

[1] B. N. Persson and A. Baratoff, Phys. Rev. B **38**, 9619 (1988).
[2] E. Turlot, D. Esteve, C. Urbina, J. M. Martinis, M. H. Devoret, S. Linkwitz, and H. Grabert, Phys. Rev. Lett. **62**, 1788 (1989).
[3] F. Capasso, K. Mohammed, and A. Y. Cho, IEEE J. Quantum Electron. **QE-22**, 1853 (1986).
[4] E. Y. Andrei, S. Yücel, and L. Menna, Phys. Rev. Lett. **67**, 3704 (1991).
[5] S. Yücel and E. Y. Andrei, Phys. Rev. B **42**, 2088 (1990).
[6] M. Y. Azbel and P. M. Platzman, Phys. Rev. Lett. **65**, 1376 (1990).
[7] J. M. Goodkind, G. F. Saville, A. Ruckenstein, and P. M. Platzman, Phys. Rev. B **38**, 8778 (1988).
[8] P. Gueret, E. Marclay, and H. Meier, Appl. Phys. Lett. **53**, 1617 (1988); Solid State Commun. **68**, 1671 (1988).
[9] E. H. Hauge and J. A. Stovneng, Rev. Mod. Phys. **61**, 917 (1989); R. Landauer, Ber. Bunsenges. Phys. Chem. **95**, 404 (1991); M. Buttiker, in *Electronic Properties of Multilayers and Low Dimensional Semiconductors,* edited by J. M. Chamberlein, L. Eaves, and J. C. Portal (Plenum, New York, 1990), p. 297.
[10] For a recent review, see E. Y. Andrei, F. I. B. Williams, C. D. Glattli, and G. Deville, *The Physics of Low Dimensional Semiconductors* (Plenum, New York, 1992).
[11] C. Grimes and G. Adams, Phys. Rev. Lett. **42**, 795 (1979); for a more accurate measurement of the melting transition, see G. Deville, J. Low-Temp. Phys. **72**, 135 (1988).
[12] D. Ceperly, Phys. Rev. B **18**, 3126 (1978); B. Tanatar and D. Ceperly, *ibid.* **39**, 5005 (1989).
[13] Y. Iye, K. Kono, K. Kajita, and W. Sasaki, J. Low-Temp. Phys. **38**, 293 (1980). See also P. Ao (unpublished).
[14] V. A. Buntar, V. N. Grigoriev, O. I. Kirichek, Yu. Z. Kovdrya, Yu. P. Monarkha, and S. S. Sokolov, J. Low-Temp. Phys. **79**, 323 (1990).
[15] H. Totsuji, Phys. Rev. B **17**, 399 (1978).
[16] Yu. M. Vil'k and Yu. P. Monarkha, Fiz. Nizk. Temp. **13**, 684 (1987) [Sov. J. Low Temp. Phys. **13**, 392 (1987)].
[17] L. V. Keldysh, Zh. Eksp. Teor. Fiz. **47**, 1945 (1964) [Sov. Phys. JETP **20**, 1307 (1965)].
[18] S. Yücel and E. Y. Andrei, Phys. Rev. B **43**, 12 029 (1991).
[19] S. Yücel and E. Y. Andrei, Phys. Rev. B **46**, 2448 (1992).
[20] P. H. Cutler, T. E. Feuchtwang, Z. Huang, T. T. Tsong, H. Nyugen, A. A. Lucas, and T. E. Sullivan, J. Phys. C **6**, 101 (1987).
[21] M. W. Cole and M. H. Cohen, Phys. Rev. Lett. **23**, 1238 (1969).
[22] C. C. Grimes, T. R. Brown, M. L. Burns, and C. L. Zipfel, Phys. Rev. B **13**, 140 (1976).
[23] M. A. Stan and A. J. Dahm, Phys. Rev. B **40**, 8995 (1989).
[24] G. Deville, A. Valdez, E. Y. Andrei, and F. I. B. Williams, Phys. Rev. Lett. **53**, 588 (1984).
[25] C. D. Glattli, E. Y. Andrei, G. Deville, J. Poitrenaud, and F. I. B. Williams, Phys. Rev. Lett. **54**, 1710 (1985).
[26] F. Gallet, G. Deville, A. Valdes, and F. I. B. Williams, Phys.

Rev. Lett. **49**, 212 (1982).
[27]Y. M. Vilk and A. Ruckenstein (unpublished).
[28]E. S. Sabisky and C. H. Anderson, Phys. Rev. A **7**, 790 (1973).
[29]F. J. de Heer and M. Inokuti, in *Electron Impact Ionization,* edited by T. D. Mark and G. H. Dunn (Springer-Verlag, New York, 1985), p. 54.
[30]M. Wanner and P. Leiderer, Phys. Rev. Lett. **42**, 315 (1979).
[31]G. T. Saville, J. M. Goodkind, and P. M. Platzman, Phys. Rev. Lett. **61**, 1237 (1988).
[32]S. Nagano, S. Ichimaru, H. Totsuji, and N. Itoh, Phys. Rev. B **19**, 2249 (1979).